Streamer depth versus vessel and seismic interference noise

Toan Dao and Martin Landrø**

ABSTRACT

For marine seismic surveying it is commonly assumed that the noise level decreases with depth. In addition, recent advances in broadband seismic have shown that greater receiver depth is beneficial in preserving low-frequency data. However, in a heavily trafficked ocean, noise from other ship including seismic interference is a counteractive process in which the noise actually increases with depth. Normal modes can be used to explain and predict the ship noise and seismic interference noise level. We find that weather noise is dominant below a frequency around the first mode's cutoff frequency (around 6 Hz), ship noise is dominant from that frequency to the upper end of the useful seismic frequency band (80 Hz). In this paper, we use a unique dataset where the streamer was towed at 8, 45 and 60 m depth in three passes over the same area in the North Sea. The water depth is 135 m on average. We observe that the noise level at 45 and 60 m depth is about 1.6 times stronger than that at 8 m. After isolating the seismic vessel noise, we find that the air gun energy is up to 46 dB stronger than the noise from the seismic vessel. However, the ocean is an effective medium to transmit sound waves, the total noise from all the ships within several hundred kilometers radius can reduce the data quality.

INTRODUCTION

Since the late 19^{th} and early 20^{th} century, ocean ambient noise has significantly increased due to anthropogenic activities. In the sea the frequency band from 10 to 200 Hz is dominated by commercial shipping (Wenz (1962), Ross (1976)) and coincides with the useful seismic data spectrum (8 - 80 Hz). The ambient noise in the ocean has increased on average 1/2 dB per year in the last few decades (Ross, 2005) due to developments both in sizes and speeds of merchant ships. Low-frequency sound experiences less attenuation and therefore propagates longer than the high-frequency sound. A 226-kiloton supertanker can produce peak spectral levels of 161 dB re µPa at 1 m for 40 - 50 Hz. Such a supertanker can be detected in the noise measured 139 - 463 km away according to Richardson et al. (1998).

Because of the presence of the free surface and the sea floor, much of the sound wave energy travels as normal modes. Normal modes or discrete modes are waves that are trapped in the water column and travel as a combination of multiple reflected and refracted waves. Unlike leaky modes or continuous modes that propagate into deeper subsurface and shorter in horizontal distance, normal modes travel along shallow interfaces and attenuate much more slowly, hence they travel longer horizontal distances. A monochromatic normal mode wave of 250 Hz attenuates 0.005 dB/km which means only one order of magnitude drop after 200 km (Luchinin, 2011). Therefore, the ship noise is always present, even when no ships are seen near the receiver (Hildebrand, 2009). Figure 1 is a snapshot of the traffic on a normal day in the North Sea generated by the automatic identification system (AIS). In reality, the traffic is even busier because there is an unknown number of ships that are not tracked by the AIS.

Noise is an integrated part of seismic data that puts huge constraints on processing and interpretation of seismic data. In time lapse seismic, data quality has been greatly improved by more accurate source and receiver positioning (Landrø, 1999). However, it has reached a plateau where it is extremely difficult to further improve repeatability due to uncontrollable noise sources other

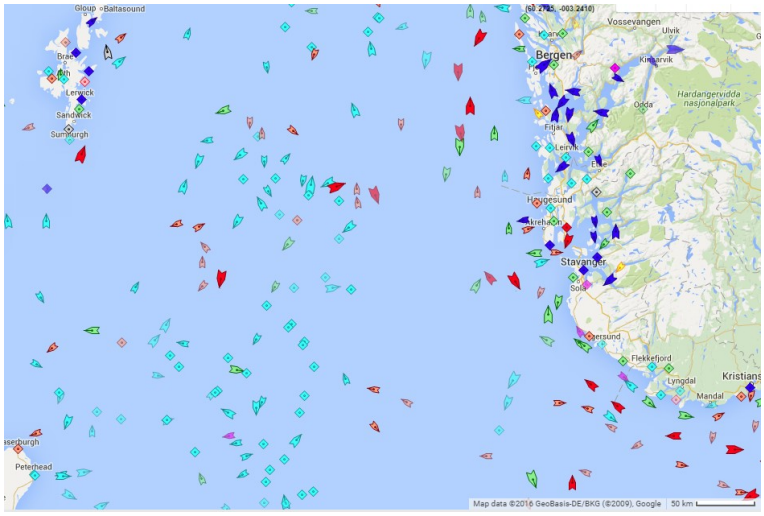

Figure 1: Typical everyday traffic in the North Sea.

than the seismic acquisition itself (Bjørlykke, 2010). Therefore, it is desirable to reduce these noise sources. Recent advances in broadband seismic which primarily attempts to preserve low frequencies are in favor of greater towing depths. Kroode et al. (2013) pointed out that the notches in the ghost spectrum depend on the streamer depth. The source depth has also been studied with respect to preserve as much low frequencies as possible (Parkes and Hegna (2011); Landrø and Amundsen (2014)). The marine environment is quieter at greater depths due to the fact that the low frequency (below 5 Hz) surface ocean noise is the dominant noise source that masks raw seismic records, decays significantly with depth. However, this effect is only valid for low frequencies, typically below 10 Hz.

We investigate the broadband noise (5-120 Hz) behavior versus depth using a unique dataset acquired offshore Norway where three different streamer depths were used: 8, 45 and 60 m. More details on the acquisition and purpose of this data set can be found in Dhelie et al. (2014). In this paper, we first consider Pekeris normal mode model (Pekeris, 1947) where a 135 m thick water layer is overlying an acoustic halfspace. The source depth is restricted to be less than 10 m since the depth of the air gun array is 7 m and the draughts of all the ships are 10 m or less. We solve the normal mode equation and predict the noise level at 8, 45 and 60 m depth. We compare the theory against the field data and develop a simple model that combines the normal modes and weather noise models to explain and be used as a tool to estimate the optimal towing depth to avoid the normal mode ship noise.

We want to stress that this paper discusses only three sources of noise: surface ocean noise, noise generated by the seismic vessel and noise generated by other vessels. Other types of noise are not discussed here. To list a few: tugging noise in the streamer (Elboth et al. (2010), Elboth et al. (2012)), noise generated by turbulent flow around the streamer (Schoenberger and Mifsud, 1974), noise generated by marine life such as whales, dolphines, croakers and pistol shrimps (Urick, 1986), high frequency ocean noise (Wenz (1962), Short (2005)) and rig noise (Fookes et al., 2005). The impact of these sources might alter and invalidate some of the findings in this paper since they are unknown and excluded.

DISPLACEMENT POTENTIAL OF NORMAL MODES

We consider a simple two-layer model as depicted in Figure 2 where the first layer represents the water column and the second layer is a halfspace. The velocity and density of each layer are denoted

as α_1, ρ_1 and α_2, ρ_2. Let c be the phase velocity, ω be the angular frequency, k_1 and k_2 be the total wavenumbers of layer 1 and 2. The displacement potential ϕ at a point in the upper layer for a given frequency and mode number is given by Ewing et al. (1957) and Pekeris (1947):

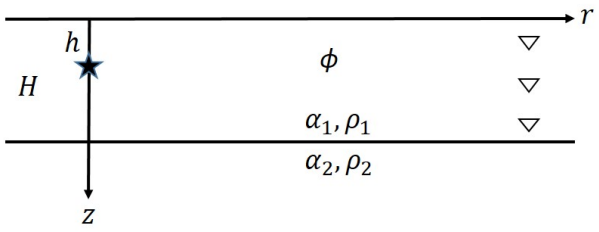

Figure 2: A two-layer model where the first layer represents the water column lying on top of a half-space that represents the seabed.

$$\phi_n(r,z,\omega) = \frac{2}{H}\sqrt{\frac{2\pi}{r}}\frac{1}{\sqrt{k_n}}V(x_n)\sin(k_{zn}h)\sin(k_{zn}H)\exp\{i(\omega t - k_{rn}r - \frac{\pi}{4})\} \tag{1}$$

where H, h, z denote water, source and receiver depth. The horizontal and vertical wavenumber of mode n, k_{rn} and k_{zn}, depend on the phase velocity c and satisfy equations 2 and 3 (Ewing et al., 1957):

$$\frac{\rho_1}{\rho_2}\tan[H(k_1^2 - k_{rn}^2)^{1/2}] = -\frac{(k_1^2 - k_{rn}^2)^{1/2}}{(k_{rn}^2 - k_2^2)^{1/2}}, \tag{2}$$

$$k_{rn}^2 + k_{zn}^2 = k_1^2. \tag{3}$$

V_n is a coefficient that corrects for the amplitude of each mode:

$$x_n = -Hk_{rn}, \tag{4}$$

$$V(x_n) = \frac{x_n}{x_n - \sin x_n \cos x_n - \frac{\rho_1^2}{\rho_2^2}\sin^2 x_n \tan x_n}, \tag{5}$$

In equation 1, the term $\sin(k_{zn}z)$ is called the mode function and depends only on the receiver depth. For a given phase velocity c, there exists multiple roots k_{rn} to equation 2: $k_{r1}, k_{r2}, .., k_{rN}$. Each wavenumber k_n corresponds a wave mode that enters equations 4, 5 and equation 1. For cases where the phase velocity $c < \alpha_1$ and $c > \alpha_2$, the right hand side of equation 2 becomes complex. As a consequence, k_{rn} also becomes complex and ϕ_n vanishes at large offset. Therefore, we are only interested in the case where $\alpha_1 \leq c \leq \alpha_2$.

To compute ϕ_n at a point (r, z) for mode n and frequency f_n , we vary the phase velocity c_n from α_1 to α_2 with a small step length δc. First, the wavenumber k_{rn} for each mode and phase velocity is calculated using equation 3. Then we define a small bin around each predefined f_n: $(f_n - \delta f, f_n + \delta f)$ and c_n: $(c_n - \delta c, c_n + \delta c)$. The potential is normalized using the total number of points falling in each bin while the recorded signal is the total contribution of all the frequencies and modes.

To illustrate normal modes, we create a model where velocities of the water layer and the seabed are 1500 m/s and 1650 m/s respectively as depicted in Figure 2. The water depth is 135 m and the density ratio between the seabed and the water column is assumed to be 1.6. Figure 3 shows the first six mode functions that correspond to the 35 Hz component which is a typical dominant frequency for the field data. In the seismic bandwidth the mode functions vary slowly and insignificantly.

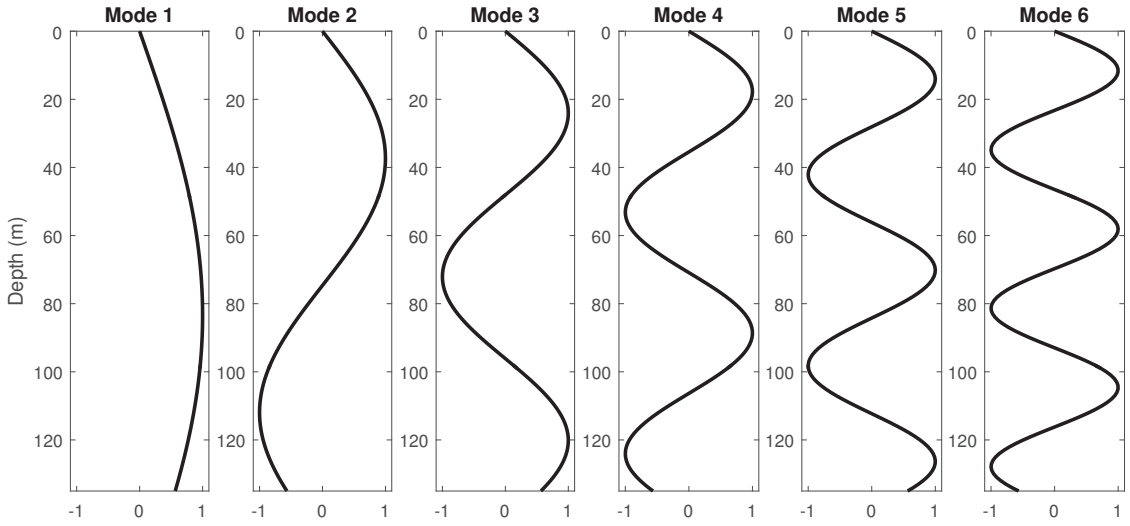

Figure 3: The mode functions for the first six modes of the model for the 35 Hz component. The mode functions resemble standing waves. At the free surface, the amplitude is always zero for all modes.

Therefore we can use these mode functions as a fairly accurate reference for qualitative amplitude interpretation. The shapes of the constituent modes resemble standing waves in space. For each mode there exists a cutoff frequency f_{nc} given by Ewing et al. (1957) above which that particular mode commences:

$$f_{cn} = \frac{(2n-1)\alpha_1\alpha_2}{4H\sqrt{\alpha_2^2 - \alpha_1^2}}. \tag{6}$$

For this model, the cutoff frequencies for the first six modes are approximately 7, 20, 33, 47, 60, 73 Hz. In reality, the cutoff frequencies can only be used as an approximation due to the heterogeneity of the media. The modes cannot be observed in unprocessed time-series data. However, because each mode travels with different phase and group velocities, they can be distinguished by time-frequency analysis. For horizontal receiver geometry such as a marine streamer, the modes are visually separable in the FK domain.

The source term plays an important role to determine the dominant modes in the data. A low frequency wave will excite only lower modes while a higher frequency wave will excite higher modes as well. The location of the receiver also has a significant impact on the contribution of each mode in the recorded wavefield. A receiver will record little or no amplitude from a mode if it is close to a node of that mode. Figure 4 shows the amplitude of mode 2 excited by the 55 Hz component received at 8, 45 and 77 m. The amplitude recorded at 77 m is in significant compared to the other two depths as 77 m is close to a node. Similarly, Figure 5 shows the amplitude of mode 3 excited by the 55 Hz received at 8, 45 and 50 m. The amplitude recorded at 8 and 45 m are almost identical and that observation agrees with the amplitude-depth relationship in Figure 3. The amplitude at 50 m is near another node. Therefore its amplitude is much weaker than that at 8 and 45 m.

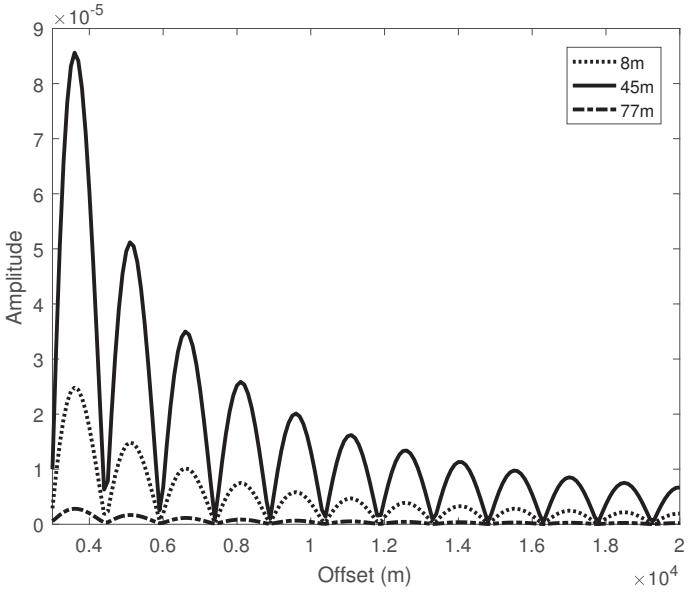

Figure 4: The amplitude contribution of the 55 Hz component to mode 2 at 8, 45 and 77 m. Note that the amplitude along offset at 77 m depth is small because a node in mode 2 exists around the depth.

FIELD DATA

Description of the data

The dataset was acquired in the North Sea over an area with a relatively flat seabed where the water depth is about 135 m. The dataset consists of three parts corresponding to streamer depths at 8, 45 and 60 m. The setup of the experiment including the source and streamer configurations is schematically portrayed in Figure 6. Table 1 shows the source and streamer setup for the experiments. Except for the different receiver depths, all acquisition parameters were kept unchanged. This was done to isolate the effect of the receiver depths on the data. A representative shot gather is plotted in Figure 7a. We extract the data with no active source from box A and with active source from box B.

Data with active source

Figure 7b shows the FK spectrum of the shot gather on the left. We observe that the first five modes (black lines) commence at a frequency close to the precomputed cutoff frequencies as given by the model. The boxed area in Figure 7b is zoomed for mode identification in Figure 7c. Figure 8 shows the rms amplitude of the traces at the far-field averaged over 2,000 shots at three depths after applying a 6 Hz lowcut filter to the data. The amplitude recorded at 45 and 60 m are of the same level and about 1.6 times stronger than that at 8 m. Figure 9 shows the average spectra at three depths normalized by the peak amplitude of the near-field recording at 8 m depth. The spectrum at 8 m for the most part is lower than that of 45 m and 60 m. The spectra of 45 m and 60 m cross over multiple times at around 16 Hz and 32 Hz. Below 16 Hz and above 32 Hz, the amplitude at 60 m is stronger than 45 m while from 16 to 32 Hz, amplitude at 45 m is stronger than 60 m. Amplitude of 8 m data starts to level with 45 m and 60 m from 60 Hz and above.

To identify the modes in the field data, we define a few narrow bandpass filters and compute

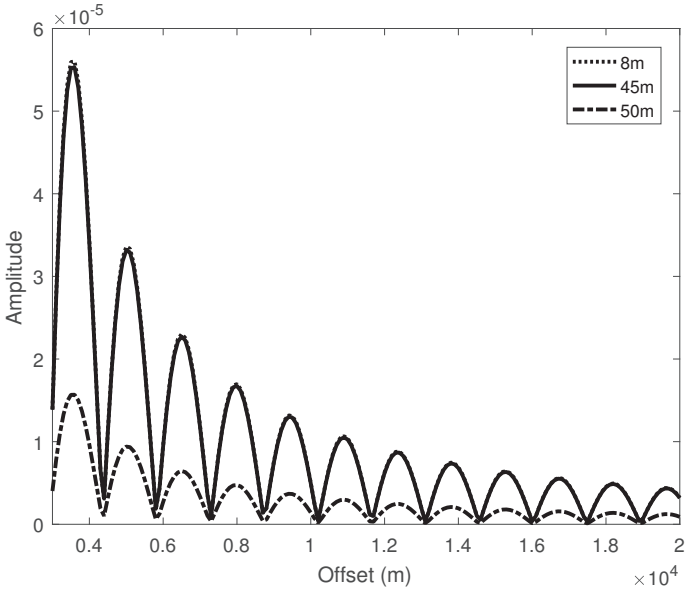

Figure 5: The amplitude contribution of the 55 Hz component to mode 3 at 8, 45 and 50 m. The amplitude at 55 m is small and significantly weaker than at the other two depths since 50 m is near a node in mode 3.

Source depth	7 m
Number of shots/streamer depth	2000
Number of guns	42
Pressure	2000 psi
Shot interval	18.75 m
Average time between shots	9 s
Number of hydrophones/group	8
Group length	12.5 m
Group interval	12.5 m
Active length	6000 m
Depth	8, 45, 60 m
Recording time	6 s
Sampling interval	2 ms
Pre-processing	2-Hz lowcut at 6 dB/oct 214-Hz highcut at 574 dB/oc

Table 1: Source and streamer configurations used in the experiments.

the rms amplitude of the filtered data. Table 2 lists the frequency bands and their excited modes. Figure 10 shows the rms amplitude of the three depths after applying the four bandpass filters. The 11-13 Hz filter is the only filter that does not contain any contribution from other modes. An excellent agreement between the predicted amplitude level and the data is observed. The amplitude at 60 m is stronger but close to that at 45 m while the amplitude at 8 m is significantly weaker. The 23-25 Hz filter also agrees with the amplitudes in mode 2 where 45 m is the strongest, followed by 60 m and 8 m which is the weakest. The relative rms amplitude levels in this band does not fit as well to the mode function as the first band because it also contains the first mode. However, the

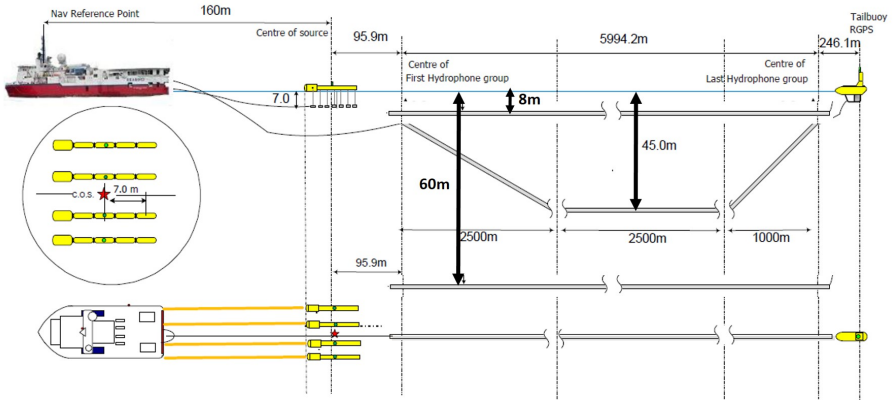

Figure 6: The streamer configurations used in the field experiments.

Frequency (Hz)	Modes
11-13	1
23-25	1, 2
35-37	1, 2, 3
47-49	1, 2, 3, 4

Table 2: Four narrow frequency bands and the modes excited.

order of magnitudes are the same as in the previous frequency band.

As frequency increases, the modes interference becomes more complex. For the last two filters, we notice that the amplitude in these frequency bands can no longer be explained by one single mode function. For the 35-37 Hz filter, the third mode function predicts that the amplitude at 8 and 60 m are similar and almost zero at 45 m. However, this band also includes mode 1 and 2. Even though there is almost no amplitude recorded at 45 m for mode 3, the amplitude at 45 m is still stronger than that at 8 m. We observe smaller differences in amplitudes between depths. Despite the fact that in this frequency band, the third mode function for 60 m depth has opposite polarity to that of mode 1 and 2, the amplitude at 60 m is still the strongest among the three depths. This observation can be explained by the source wavelet. Although the source wavelet in these experiments is unknown, we can guess the peak frequency using the spectrum of the near-field in Figure 9. In the field data with active source, the dominant frequencies are roughly from 35-60 Hz. The 35-37 Hz components are much stronger than the 11-13 Hz and 23-25 Hz components. The result is that the pressure recorded for mode 3 at 60 m overcomes its positive amplitude of mode 1 and 2. As a result, the amplitude at 60 m is the strongest while the amplitude at 8 m is steadily increasing. In the last bandpass filter, 45 m is near a negative antinode of mode 4. The receivers at this depth do not record any pressure in mode 3. Again, the near-field spectrum suggests that the source is strongest in the 47-49 Hz band (black curve in Figure 9). The final result is the negative amplitude at mode 4 overcomes the positive amplitudes in mode 1 and 2. The receivers at 60 m gain more negative contribution from mode 4 and 8 m continue to receive some more positive amplitude.

Data with no active seismic source

Figure 11 shows a representative noise record at far offset. The first gather shows curved events that suggest that the noise source is near and makes a very small broadside angle to the streamer. Though the time-offset gather is completely masked by these event, the FK spectrum reveals events

with different apparent velocities. The event with apparent velocity equal to the same as water velocity is identified as seismic vessel noise. Seismic interference from another seismic vessel in the opposite direction can be identified in the FK domain. Swell and vibration noise dominate the lower frequency spectrum. The vibration noise travelling at 50 m/s in the streamer and highly aliased due to group forming. Part of the energy in seismic vessel noise and seismic interference can also be tugging and vibrations traveling at approximately water velocity along the streamer cover. In Figure 12, the seismic interference is dominant. Its coherency allows us to identify some of the modes in the FK spectrum. Again, the seismic vessel noise, swell and vibration noise are visible in the FK domain. The seismic vessel noise is always present and quite stable in all the gathers. Its visibility in the time domain depends on the strengths of other noise sources. However, it is always visible in the FK domain. We show an example where the seismic vessel noise is strong in the time domain in Figure 13. In this gather, we can identify some of the modes in the amplitude in the FK domain.

Figure 14 shows the spectra of the noise data for the three depths. At frequencies below 6 Hz, near the cutoff frequency of mode 1, the seismic record is dominated by a combination of the surface ocean noise, turbulence interaction with the streamer, lean-in cable, birds and other equipments. In this lower end of the frequency band, the amplitude at 8 m is larger than those at 45 and 60 m. Above 6 Hz, the noise is dominated by normal modes. This interpretation is based on observed similarities between theory and data. The traffic in the area where the data were acquired is always heavy. We monitored the traffic density over a course of a few days and observed that the traffic density was stable. If the assumptions that the ship traffic is the same to all three experiments and the weather noise variation above 6 Hz is negligible are valid, we can conclude that the noise level above the first cutoff frequency is minimal at 8 m compared to the other two depths.

Having confirmed that seismic vessel noise is a common noise source in all three streamer datasets, we attempt to separate this noise using a fan filter that removes all events with apparent velocities outside the range from 1400 to 1700 m/s. Figure 15 shows the rms amplitude of all the noise combined from 6 Hz and above prior to applying the fan filter. Again, the average noise level at 8 m is lower than at 45 and 60 m. The peak at 8 m around shot 1,600 is not fully understood. A reasonable explanation could be a passing ship or seismic interference noise. Figure 16 shows the rms amplitude of the seismic vessel dominated noise obtained after applying the fan filter. The rms amplitude between all the noise sources combined is 6-10 times stronger than the seismic vessel noise. The amplitude ranges of the seismic vessel dominated noise at 45 and 60 m are roughly the same and 1.6-1.7 times stronger than at 8 m. The broad peak in the rms amplitude of the 60 m data is most likely due to an increase in activity of ships and vessels ahead of the sail line.

A similar ratio of 1.7 was established earlier in the paper when we considered the data with air gun signature (Figure 8). We observe that in this particular case, the seismic vessel dominated noise is about 46 dB weaker than the amplitude of the air gun source. Despite that the noise from the seismic vessel is very weak compared to the air gun, the total noise from all the ships and seismic interference in the area will impact the data quality.

Combination of weather noise and normal modes models

Wenz (1962) developed an empirical weather noise model based on the lowest observed noise levels at different locations, weather conditions and times of year. In the seismic frequency band, the weather noise can be modeled using a simple logarithmic function. Let wn_a and wn_b be the weather noise at 8 and 60 m:

$$wn_a(f) = Ae^{-a(f-f_0)} \tag{7}$$

$$wn_b(f) = Be^{-b(f-f_0)} \tag{8}$$

where $f \geq f_0$, f is the frequency, f_0 is the frequency below which the weather noise is more dominant. A, a and B, b are coefficients that describe the magnitude and the decaying rate of the weather noise at 8 and 60 m. We are not interested in frequencies below f_0 as there is very little or no normal modes and we know that the weather noise at 8 m is greater than that 60 m.

To compute the difference in frequency spectra of the normal modes at two depths 8 and 60 m, we choose the source wavelet to be identical to 1 for simplicity. We need to pick a set of parameters that satisfy the conditions that the amplitude at 8 m are greater than that at 60 m. The decaying rate is assumed to be constant for both depths. We set $A = 5$, $B = 1$, $a = b = 0.8$ and $f_0 = 3$. Figure 17 shows the difference between 8 and 60 m in modeled normal mode (left), weather noise (middle) and the combination of both (right). The field data curve is obtained by taking the difference between the spectra of 8 and 60 m in Figure 14. The combined model and field data are normalized first by their L2-norms and then by the peak amplitudes for comparison. In practice, this step is equivalent to calibration of the noise sources. We observe similar trends in the average difference between two depths in the model and field data. The combined frequency model and the field data indicates that below a certain frequency, the noise recorded at 8 m is stronger than at 60 m. However, in the useful seismic bandwidth (8 - 80 Hz), the noise at 8 m is weaker than at 60 m. From 80 to 120 Hz, the noise levels at two depths are comparable.

DISCUSSION

In this paper we rely on the fact that the noise in the area is mainly influenced by ship noise, seismic interference noise and weather noise. We ignore other noise sources such as turbulence, flow, earthquakes, marine animals and other acquisition-related noise. This probably explains the high anomaly observed in the rms amplitude of the seismic vessel noise at 60 m in Figure 16. Our model simplifies the ocean environment in which we assume homogeneous water layer and seabed. Temperature and salinity are the main parameters that determine the water velocity and density. Water velocity and density variations are usually ignored in marine seismic. This study also depends on the flat bathymetry which enables us to analytically solve for the mode functions. Normal modes for heterogeneous media and more complex boundaries can be modeled numerically but not necessary in our study. The modeling parameters were chosen based on the prior knowledge of the area. Qualitatively, the mode functions are quite insensitive to model's parameters. For hard seabed where seabed density and velocity are high, most of the energy is trapped in the water column. In this case, the bottom ends of all the mode functions shift toward zero and normal mode energy recorded at the seabed is insignificant. Figure 18 shows the modeled difference in frequency content between the normal mode signals received at 8 and 60 m when the water depth varies. The receivers are placed 50 km away from the source. The modeling takes into account the number of mode existing up to 120 Hz: 4 modes for 75 m, 15 modes for 300 m and 145 modes for 3,000 m. We find that in the seismic bandwidth, the signals at 8 m is almost always weaker than those at 60 m. It is worth noting that incorporating an accurate sea water velocity profile will help to make a better prediction on normal mode noise. In reality, sea water velocity is heterogeneous and changes seasonally. Sound Fixing and Ranging (SOFAR) channel is a layer in the water column where the sound speed is minimum. Energy radiated by a source in this layer can be recorded thousands of kilometers away (Jensen et al., 2000). It is important to stress that the normal mode signal created by the source in a marine seismic experiment is not a problem for seismic imaging and our focus in this paper is the background normal mode noise created by other noise sources in the water column.

Since the air gun array generates a lot of energy, the question of the noise from previous shots is raised especially when the time between two shots is short. Landrø (2008) used a 30-second-long trace recorded 2,600 m away from the source to infer the relationship between amplitude and time between shots. In Figure 19, the background noise level is the lower end of the rms amplitude curve after the source has been fired for 20 seconds. The difference between the amplitude level around the shot interval (9 seconds) and the background noise level is referred as the shot generated noise. This noise is about 10 dB stronger than the background noise. It was also shown that this relationship is consistent with respect to the source. This noise cannot contain any normal modes from the air gun array since they have already passed that location some time before. Therefore it is greatly attenuated in the subsurface. In addition, its apparent velocity is usually not the same as that of the normal modes from the seismic vessel or the air gun array.

CONCLUSION

We have shown that the normal modes can explain the distribution of noise level in presence of ship noise including seismic interference noise in the ocean. While lowering the receivers helps avoiding low-frequency weather noise and preserving low-frequency signals, normal modes from different noise sources act as a counteractive process. The mode functions can be used to predict the contribution of each mode to the recorded pressure. When the source is known, the normal mode contribution generated by the source itself can be calculated. We find that below the first normal mode cutoff frequency the shallow streamer depth contains more noise than deeper depth and above this frequency, the opposite occurs. A major part of the noise above this cutoff frequency can be explained by normal modes originating from ship traffic in the area and noise generated by the seismic vessel itself.

In the field data, due to dispersion, it is straightforward to identify the modes in the FK spectrum. In the time domain, it is harder to observe these modes. The amplitude difference between various sources are as follows: the amplitude above 6 Hz of 45 and 60 m is 1.6 - 1.7 times stronger than that of 8 m for both active and non-active source data. The seismic vessel dominated noise is about 46 dB weaker than the air gun data. However in heavy traffic where hundreds or thousands of ship are in a radius of several hundreds of km, the total effect of normal mode ship noise will have an impact on the data.

The combination of the normal modes and weather noise model fits with the field data in the sense that their overall trends agree. The rapid oscillations in the field data are not captured in the model due to the assumptions made earlier. That is we only consider ocean background noise, seismic interference and ship noise including the noise from the seismic vessel itself. To reduce the amount of normal mode noise, this study shows that a shallow (8 m) towing depth is more optimal than deeper towing depths (45 and 60 m).

ACKNOWLEDGEMENT

We thank Lundin AS for providing the data and allowing us to publish the result, especially Per-Eivind Dhelie for accommodating all our data-related requests. We thank Thomas Elboth, Mike Norris and an anonymous reviewer for their comments and suggestions that helped greatly to improve the manuscript. We thank Hefeng Dong for valuable discussions on marine acoustics. We acknowledge Norwegian Research Council for funding the ROSE consortium at NTNU.

REFERENCES

Bjørlykke, K., 2010, Petroleum geoscience: From sedimentary environments to rock physics: Springer-Verlag Berlin Heidelberg.

Dhelie, P., J. E. Lie, V. Danielsen, A. K. Evensen, and A. Myklebostad, 2014, Broadband seismic a novel way to increase notch diversity: SEG Technical Program Extended Abstract, 148152.

Elboth, T., D. Lilja, B. A. P. Reif, and O. Andreassen, 2010, Investigation of flow and flow noise around a seismic streamer cable: Geophysics, **75**, Q1–Q9.

Elboth, T., B. A. P. Reif, O. Andreassen, and M. B. Martell, 2012, Flow noise reduction from superhydrophobic surfaces: Geophysics, **77**, P1–P13.

Ewing, W. M., W. S. Jardetsky, and F. Press, 1957, Elastic waves in layered media: McGraw-Hill.

Fookes, G., C. Warner, and B. R. V., 2005, Practical interference noise elimination in modern marine data processing: IEEE Journal of Oceanic Engineering, **30**, 257–261.

Hildebrand, J. A., 2009, Anthropogenic and natural sources of ambient noise in the ocean: Marine Ecology-Progress Series, **395**, 5–20.

Jensen, F., W. A. Kuperman, M. B. Porter, and H. Schmidt, 2000, Computational ocean acoustics: Springer Science & Business Media.

Kroode, F. t., S. Bergler, C. Corsten, J. W. de Maag, F. Strijbos, and H. Tijhof, 2013, Broadband seismic data the importance of low frequencies: Geophysics, **78**, WA3–WA14.

Landrø, M., 1999, Repeatability issues of 3-D VSP data: Geophysics, **64**, 1673–1679.

———, 2008, The effect of noise generated by previous shots on seismic reflection data: Geophysics, **73**, Q9–Q17.

Landrø, M., and L. Amundsen, 2014, Is it optimal to tow air-guns shallow to enhance low frequencies?: Geophysics, **79**, A13–A18.

Luchinin, A. G., 2011, Low-frequency ocean acoustics: Vestnik Rossiiskoi Akademii Nauk, **81**, 204–214.

Parkes, G. E., and S. Hegna, 2011, How to influence the low frequency output of marine air-gun arrays: EAGE Extended Abstract, H012.

Pekeris, C. L., 1947, Theory of propagation of explosive sound in shallow water: Geological Society of America Memoir, **27**, 1–117.

Richardson, J. W., C. R. Greene, C. I. Malme, and D. H. Thomson, 1998, Marine mammals and noise: Academic Press.

Ross, D., 1976, Mechanics of underwater noise: Pergamon Press, New York.

———, 2005, Ship sources of ambient noise: IEEE Journal of Oceanic Engineering, **30**, 257–261.

Schoenberger, M., and J. F. Mifsud, 1974, Hydrophone streamer noise: Geophysics, **39**, 781–793.

Short, J. R., 2005, High-frequency ambient noise and its impact on underwater tracking ranges: IEEE Journal of Oceanic Engineering, **30**, 267–274.

Urick, R. J., 1986, Ambient noise in the sea: The Journal of the Acoustical Society of America, **86(4)**.

Wenz, M. G., 1962, Acoustic ambient noise in the ocean: Spectra and sources: The Journal of The Acoustical Society of America, **34**, 1936–1951.

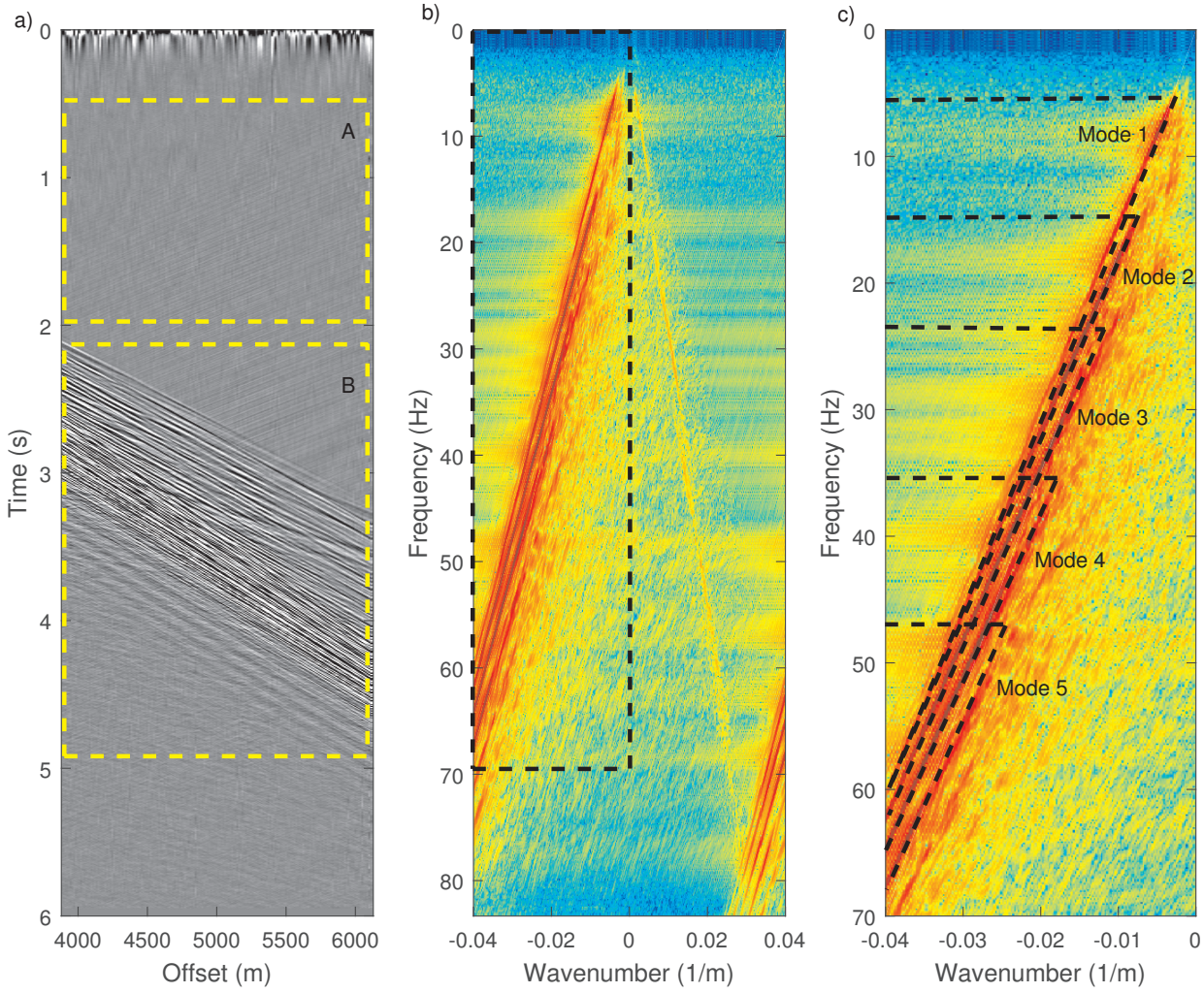

Figure 7: Part of a shot gather at far offset in a) time domain and b) FK domain computed from the entire gather. Box A is where the noise data is extracted and box B is the active source data. The FK spectrum in the black box in b) is zoomed in in c) for interpretation of the modes. Mode 1 to 5 can be distinguished in the FK spectrum. Each of them starts at a cutoff frequency close to a theoretically precomputed cutoff frequency given by the model and travels at a different group velocity.

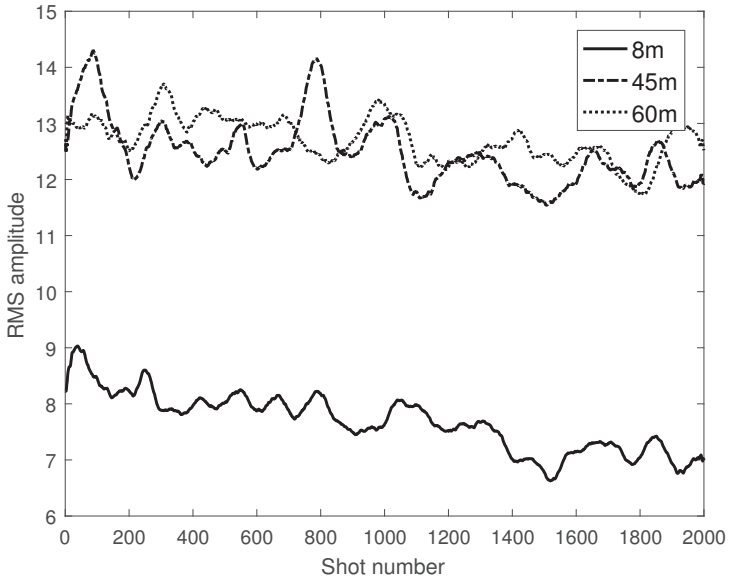

Figure 8: Average rms amplitude over 2000 shots of the far offset data extracted in box B in Figure 7 for 8, 45 and 60 m after applying a 6 Hz lowcut filter.

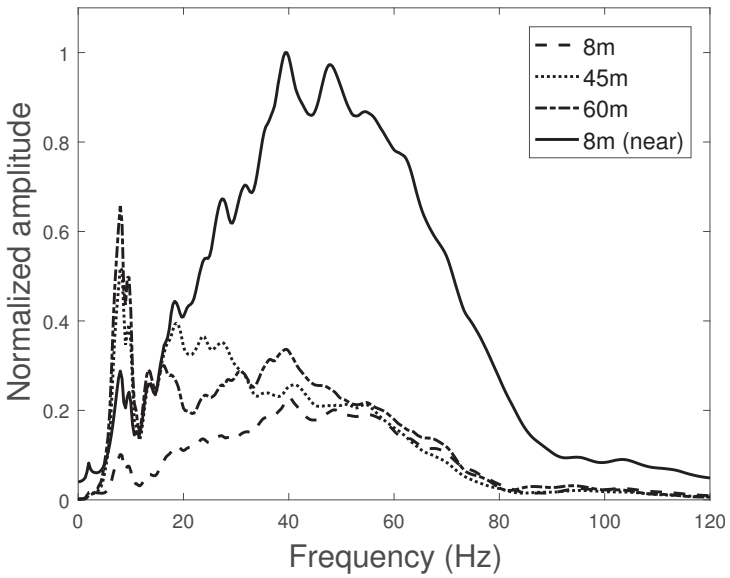

Figure 9: Frequency spectra of the far offset data extracted in box B in Figure 7 and near offset data of 8 m data. The spectra are normalized by the peak amplitude of the near offset data at 8 m.

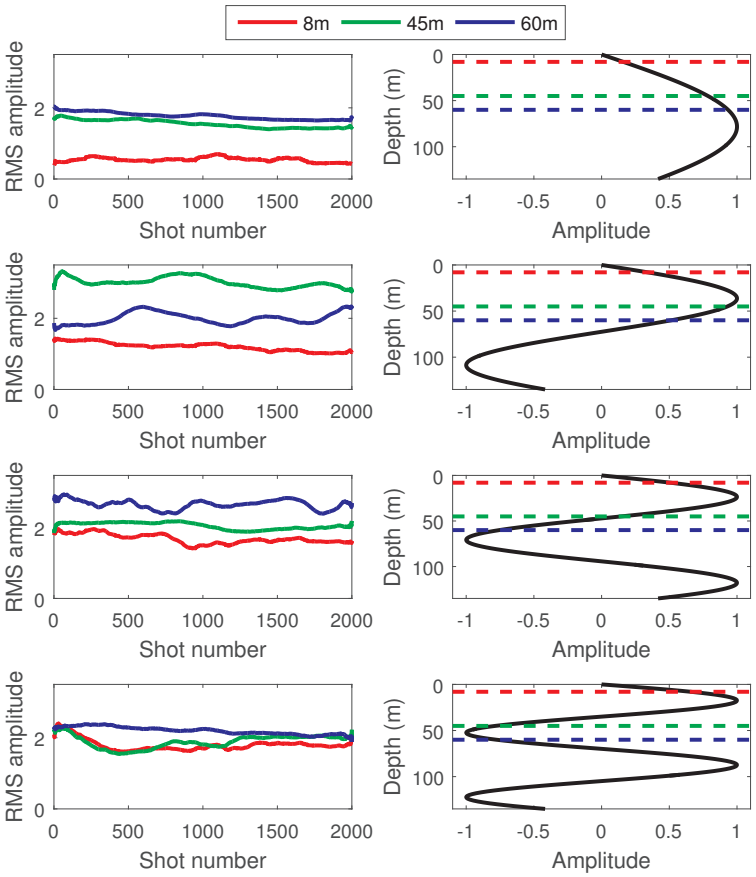

Figure 10: From top to bottom, the rms amplitude of the far offset data with active source after applying bandpass filters 11-13 Hz, 23-25 Hz, 35-37 Hz, 47-49 Hz. The mode functions corresponding to the frequency bands are shown to help visualize the relative amplitudes between three different depths.

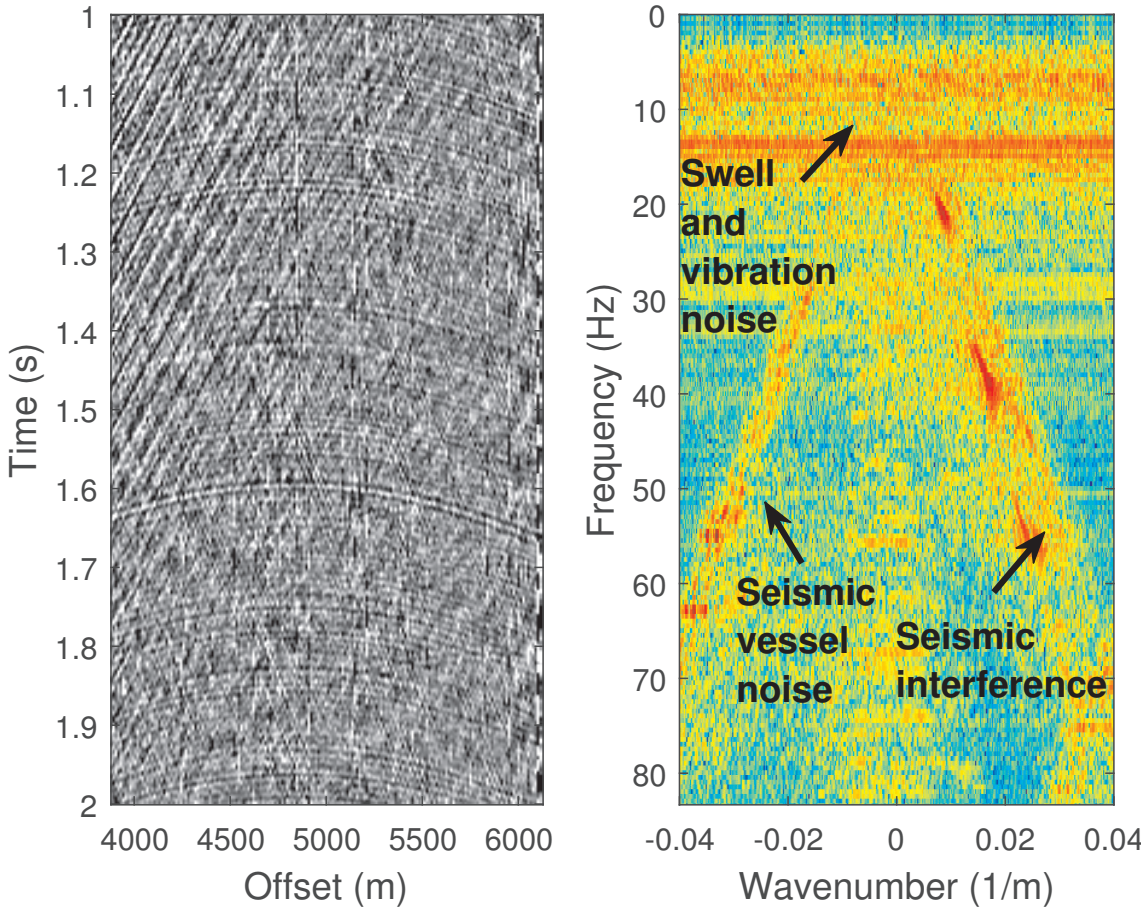

Figure 11: A representative noise gather when a ship noise is passing nearby. The events in the time domain are curved. Seismic vessel noise and seismic interference can be identified in the FK domain. Swell and vibration noise dominate the lower frequency spectrum.

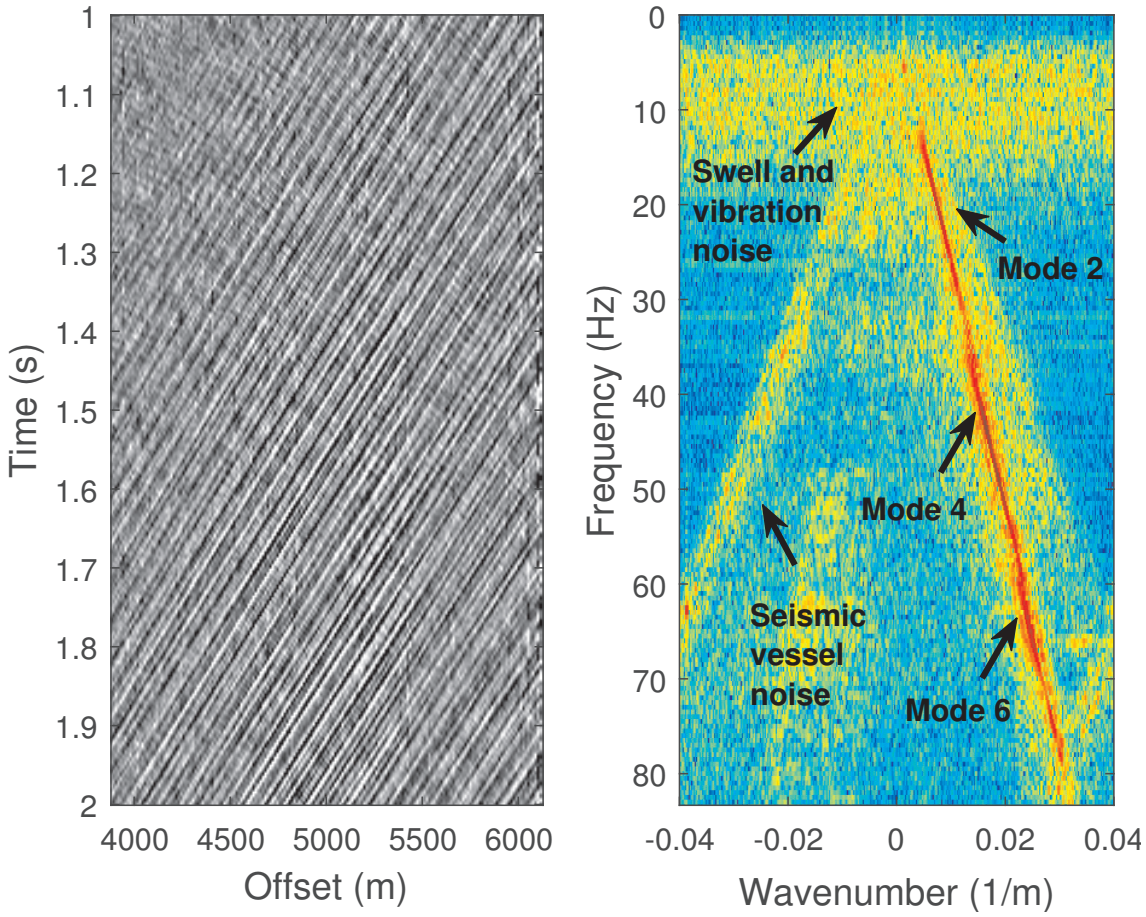

Figure 12: A representative noise gather where seismic interference is dominant and coming from the opposite direction to the towing direction. Mode 2, 4 and 6 can be identified. Seismic vessel noise, swell and vibration noise are visible in the FK domain.

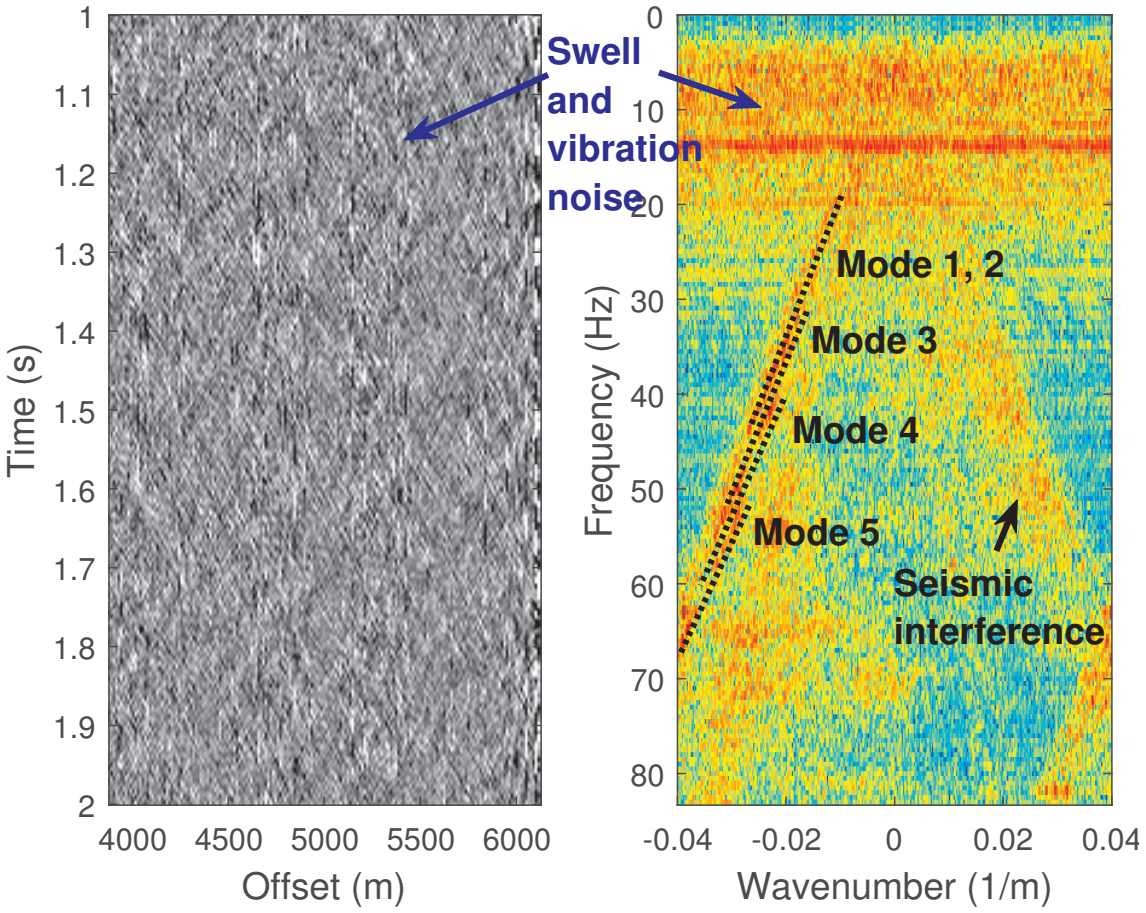

Figure 13: A representative noise gather where the seismic vessel noise is strong. The first five modes can be interpreted. Swell and vibration noise can be identified in both time and FK domain. Seismic interference is visible in the FK domain.

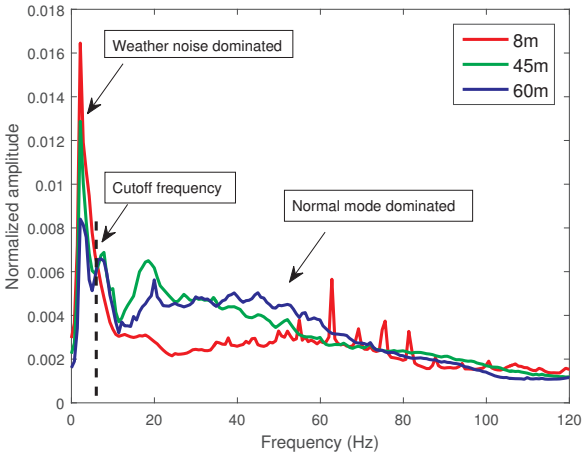

Figure 14: Frequency spectra of the noise data extracted from Box A in 7 at different depths. The spectra are normalized using the peak amplitude of the spectrum of the near offset data with active source at 8 m depth. Below 6 Hz, the noise is dominated by the weather. Above 6 Hz, normal mode noise dominates the noise spectra.

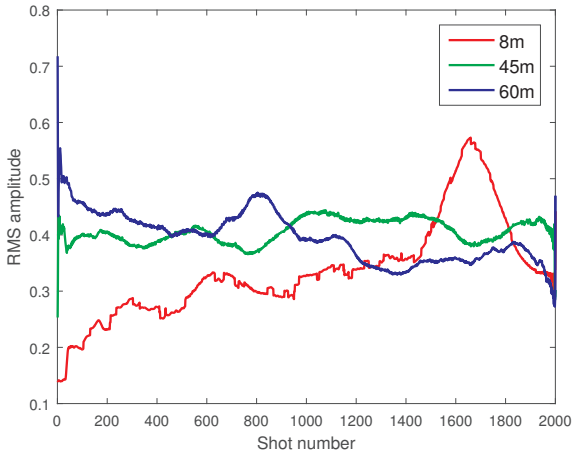

Figure 15: RMS amplitude of the noise data extracted from Box A in Figure 7 after applying a 6-Hz lowcut filter to remove the weather-dominated noise.

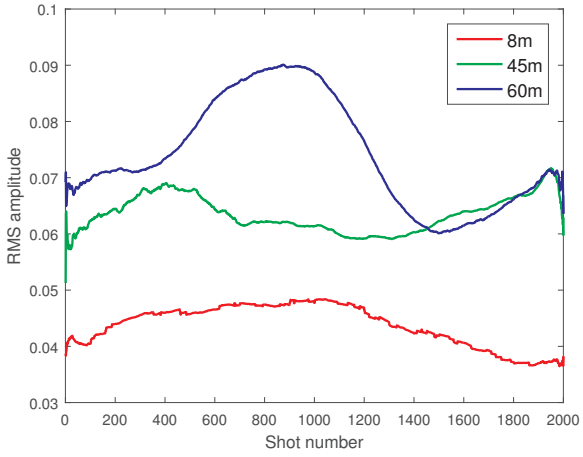

Figure 16: RMS amplitude of the seismic vessel noise extracted from the noise data using a fan filter that accepts events with apparent velocity ranges from 1400 to 1700 m/s.

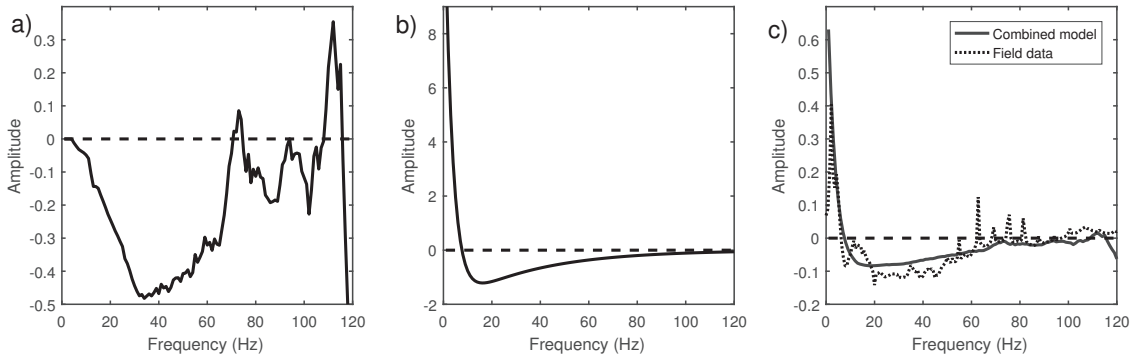

Figure 17: a) The modeled difference in frequency between 8 and 60 m in normal modes, b) the weather noise, c) the combined model and the field data after the curves are normalized by their L2-norms for comparison.

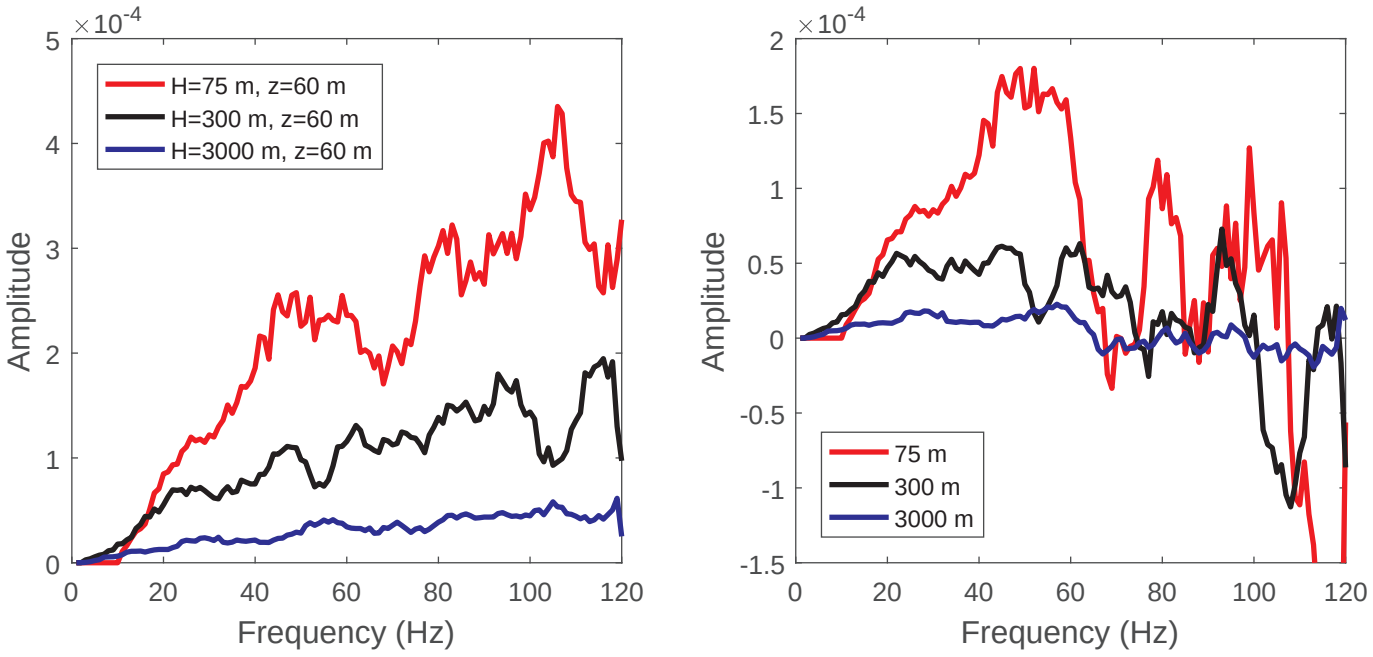

Figure 18: The modeled normal mode signals received at 60 m (left) and the differences between normal mode signals received at 8 and 60 m (right) when the water depth is 75, 300 and 3,000 m.

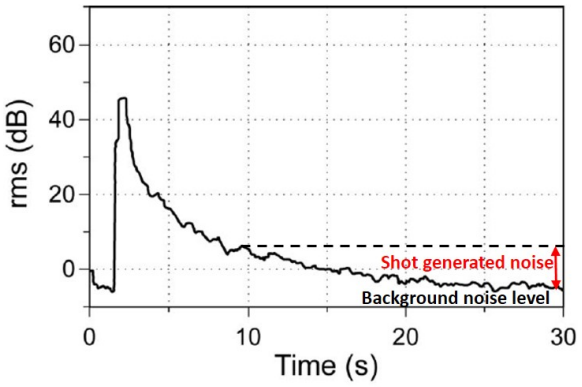

Figure 19: RMS amplitude of a long trace computed using a sliding window to infer the relationship between shot interval and shot gun generated noise (modified from Landrø (2008)).